



## GyneScan: An Improved Online Paradigm for Screening of Ovarian Cancer via Tissue Characterization

www.tcrt.org

DOI: 10.7785/tcrtexpress.2013.600273

Ovarian cancer is the fifth highest cause of cancer in women and the leading cause of death from gynecological cancers. Accurate diagnosis of ovarian cancer from acquired images is dependent on the expertise and experience of ultrasonographers or physicians, and is therefore, associated with inter observer variabilities. Computer Aided Diagnostic (CAD) techniques use a number of different data mining techniques to automatically predict the presence or absence of cancer, and therefore, are more reliable and accurate. A review of published literature in the field of CAD based ovarian cancer detection indicates that many studies use ultrasound images as the base for analysis. The key objective of this work is to propose an effective adjunct CAD technique called *GyneScan* for ovarian tumor detection in ultrasound images. In our proposed data mining framework, we extract several texture features based on first order statistics, Gray Level Co-occurrence Matrix and run length matrix. The significant features selected using *t*-test are then used to train and test several supervised learning based classifiers such as Probabilistic Neural Networks (PNN), Support Vector Machine (SVM), Decision Tree (DT), *k*-Nearest Neighbor (KNN), and Naïve Bayes (NB). We evaluated the developed framework using 1300 benign and 1300 malignant images. Using 11 significant features in KNN/PNN classifiers, we were able to achieve 100% classification accuracy, sensitivity, specificity, and positive predictive value in detecting ovarian tumor. Even though more validation using larger databases would better establish the robustness of our technique, the preliminary results are promising. This technique could be used as a reliable adjunct method to existing imaging modalities to provide a more confident second opinion on the presence/absence of ovarian tumor.

Key words: Ovarian cancer; Computer aided diagnosis; Texture analysis; Ultrasound; classification; Feature extraction; Tissue characterization; Screening.

### Introduction

Nowadays, ovarian neoplasm cancers represent a significant health problem in industrialized nations with the female population that has a 2.5% lifetime chance of developing ovarian cancer (1, 2). Between the age group 55 to 74 years, more than 50% of ovarian cancer deaths happen, and around 25% of deaths occur between 35 and 54 years (3, 4). It is the fifth highest reason for cancer in women (affecting about 1 out of 70 women) and the leading cause of death (1% of all women die of it) from gynecological cancers (5). The incidence of this cancer is higher in developed countries owing to lifestyle and heredity factors (6). Many heredity

**Abbreviations:** CAD: Computer Aided Diagnosis; PNN: Probabilistic Neural Networks; SVM: Support Vector Machine; DT: Decision Tree; KNN: *k*-Nearest Neighbour; NB: Naïve Bayes; TVUS: Transvaginal Ultrasonography; GLCM: Gray Level Co-occurrence Matrix.

**U. Rajendra Acharya, Ph.D.,  
D.Eng.<sup>1</sup>  
S. Vinitha Sree, Ph.D.<sup>2</sup>  
Sanjeev Kulshreshtha, M.Tech.<sup>2</sup>  
Filippo Molinari, Ph.D.<sup>3\*</sup>  
Joel En Wei Koh, B.Sc.<sup>1</sup>  
Luca Saba, M.D.<sup>4</sup>  
Jasjit S. Suri, M.S., Ph.D.,  
M.B.A., Fellow AIMBE<sup>5,6†</sup>**

<sup>1</sup>Department of Electronics and Computer Engineering, Ngee Ann Polytechnic, Singapore

<sup>2</sup>Visiting Scientist, Global Biomedical Technologies, CA, USA

<sup>3</sup>Biolab, Department of Electronics and Telecommunications, Politecnico di Torino, Torino, Italy

<sup>4</sup>Vascular Screening and Diagnostic Centre, London, and Department of Biological Sciences, University of Cyprus, Nicosia, Cyprus

<sup>5</sup>Point of Care Devices, Global Biomedical Technologies, Inc., Roseville, CA, USA; Diagnostic and Monitoring Division, AtheroPoint(TM) LLC, Roseville, CA, USA

<sup>6</sup>Department of Electrical Engineering, Idaho State University (Affl.), Idaho, USA

†All reprint correspondence.

\*Corresponding author:  
Prof. Filippo Molinari, Ph.D.  
Phone: +39 11 564 4135  
E-mail: filippo.molinari@polito.it

factors are associated with ovarian cancer occurrence risk, in particular age (7) and the presence of harmful mutations in tumor suppressor BRCA1 or BRCA2 genes (7, 8).

The rapid and precise diagnosis of cancer pathology is extremely important to offer a better survival rate to the affected women, and, in this setting, imaging analysis represents a key technique. Currently, three main techniques are used to image adnexa: Ultrasound (US), Computed Tomography (CT) and Magnetic Resonance (MR) (1, 9-12). CT, MR, and radioimmunoscinigraphy have one or more of the following limitations: cost, device availability, radiation exposure. The appearances of both the normal and cancerous ovaries on ultrasound images have been studied since the use of pelvis ultrasound (13-15). Barua *et al.* (15) have recently studied the feasibility of a preclinical animal model in determining the effectiveness of contrast enhanced ultrasonography in detecting early stage ovarian cancer. Transvaginal Ultrasonography (TVUS) is the first-choice technique ovarian neoplasm characterization because of the excellent temporal and spatial resolution and the absence of risk related to radiation and the administration of contrast material (16).

With the introduction of TVUS and 3D-ultrasonography, the sensitivity and specificity of ultrasonography have been shown to have improved significantly (17, 18). However, the effectiveness of ultrasonography is mainly related to the level of expertise of the reader (19), and in one study, it was observed that the most experienced sonographer obtained an accuracy of 92%, and the less experienced observers had only an accuracy in the range of 82% and 87% (20). Furthermore, studies (21) have shown that the nature of benign and malignant ovarian tumors may sometimes overlap in the acquired images, and thereby, make it difficult for the ultrasonographers or physicians to detect the exact type of tumor. Such ambiguous appearances result in unnecessary biopsies, which increase cost, time, and patient anxiety. Therefore, there is a need for an adjunct modality that could provide more objective information on the nature of the tumor.

Over the past few years, techniques for the Computer Aided Diagnosis (CAD) of specific pathologies have been proposed for more objective determination of the presence/ absence of disease and for the improvement of differential diagnosis of lesions (22-24). These techniques generally select features that quantify the grayscale intensity variations in the images and use them to develop classifiers that automatically detect the presence of disease. Due to the minimal involvement of human interpretation in the entire protocol, such CAD based techniques can provide objective and reproducible results. Most of CAD studies for ovarian cancer detection use features based on (a) blood test results (25) (b) Mass Spectrometry (MS) data (26-28) and (c) ultrasound images (29-31). The curse of dimensionality issue affected the MS based studies

(32) as they have to study a huge amount of features extracted from a relatively small dataset. Ultrasound is currently a very commonly offered affordable technique. A literature review of ultrasound-based techniques describes that there is still room for improvement in the detection accuracy. Therefore, in this work, we have proposed a CAD technique for ovarian tumor classification in ultrasound images. Comprehensive morphological characteristics of malignant and benign tumors can be evaluated by 3D ultrasonography compared to 2D ultrasonography (33). Even though some studies have concluded that 3D ultrasound did not have a better diagnostic performance than its 2D counterpart (34, 35), few other studies have indicated that power Doppler ultrasound and the selective use of 3D ultrasonography can improve the accuracy of ovarian tumor diagnosis (36, 37). Hence, in this work, we have developed our protocol using images acquired using 3D transvaginal ultrasound.

## Methods

### Data

In the present work, twenty non-consecutive women with previous diagnosis of ovarian mass (10 malignant, 10 benign; nine post-menopausal, eleven pre-menopausal; age: 29 to 74 years) were evaluated. The study was approved by the Institutional Review Board and the procedure was explained to each woman before obtaining informed consent. One of the authors of this paper consecutively selected these women during pre-surgical evaluation. Women with no anatomopathological evaluation were excluded from the study. First these subjects were scanned by B-mode ultrasonography to study the adnexal masses. Subsequently, the imaged masses were subdivided into unilocular, multilocular, unilocular-solid, multilocular-solid or solid. The tumor vascularization was evaluated by 2D power Doppler. To minimize noise, the power Doppler setting was specifically tuned for each subject in order to obtain maximum sensitivity while avoiding artifacts.

Prior to surgery, all the patients underwent 3D-transvaginal ultrasonography evaluation, and 3D volumes of the suspicious areas were acquired. Depending on the size of the volume box, the acquisition time varied between two and six seconds. In the case where more than one volume was recorded for an adnexal mass, only the first volume was used for further analysis. We wanted our database to contain 1300 benign and 1300 malignant images to build and evaluate the classifiers. Therefore, we selected the middle 130 images from each 3D volume acquired from each of the 10 benign and 10 malignant subjects, thus making our database to have 1300 malignant and 1300 benign images. To obtain the Region of Interest (ROI), the image was cropped automatically using the horizontal and vertical gradients to detect the boundaries of the black frame border around the image. Subsequently, we captured images of the size of  $256 \times 256$  and a gynecologist

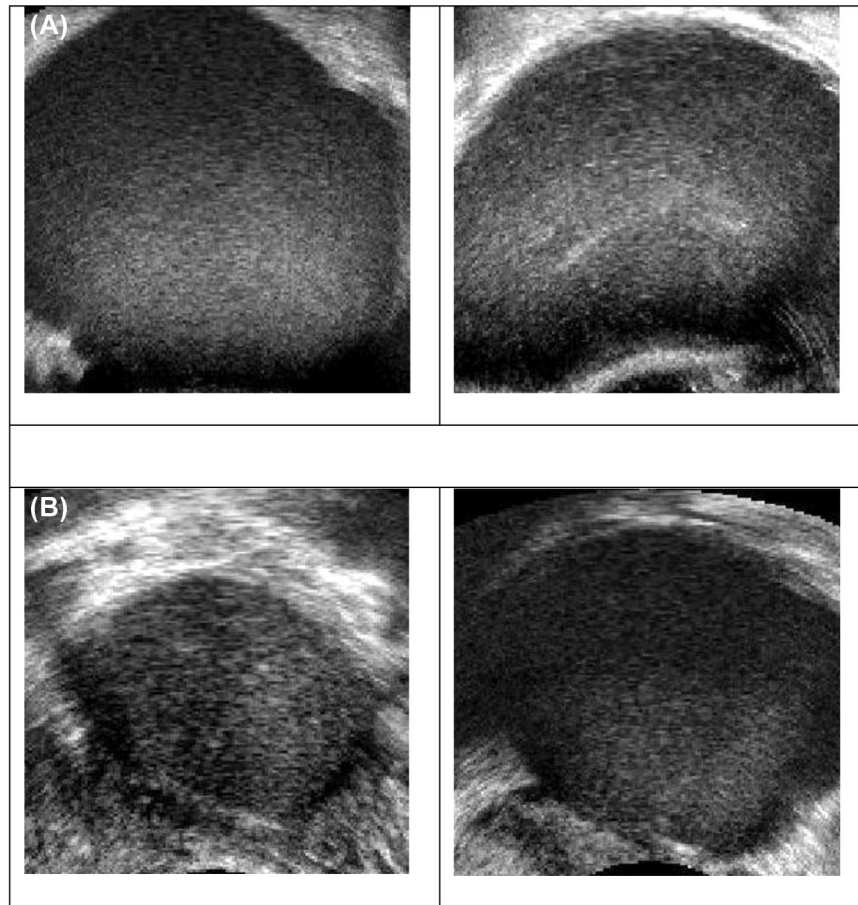


**Figure 1:** Sample ultrasound images of (A) benign ovarian tumor (upper panels) (B) malignant ovarian tumor (bottom panels).

and radiologist marked out the squared ROI from individual cropped images. Figure 1 depicts a few examples of ultrasound images of benign and malignant ovarian tumors.

*Overall GyneScan Architecture*

Our proposed system for ovarian tumor classification *GyneScan* is presented in Figure 2. The on-line classification system part of the figure indicates the steps in processing a test/new patient image. This system determines the class of the test image (benign/malignant) by using the features extracted from the test image in the classifiers that have already been trained by using the training parameters assessed by the off-line learning system. The off-line classification system evaluates the training parameters of the classifiers by using the combination of the features extracted from the training dataset and the corresponding ground truth training class labels. In this work, we developed and evaluated the following classifiers: Probabilistic Neural Networks (PNN), Support Vector Machine (SVM), Decision Tree (DT), *k*-Nearest Neighbor (KNN), and Naïve Bayes (NB) using stratified ten-fold cross-validation. By comparing the

predicted class labels of the test images and the corresponding ground truth labels, various performance measures (accuracy, sensitivity, specificity, and Positive Predictive Value (PPV)) were calculated for each classifier.

*Texture based Features Extraction*

We used Gray Level Co-occurrence Matrix (GLCM) (38) and the run length matrix (39) texture methods for feature extraction. Let the image be represented by a  $M \times N$  gray-scale matrix  $I(i, j)$ , where each element of the matrix indicates the intensity of a single pixel in the image. The co-occurrence matrix  $C(i, j | \Delta_x, \Delta_y)$  is the second-order probability function estimation. This matrix denotes the rate of occurrence of a pixel pair with gray levels  $i$  and  $j$ , given the distances between the pixels are  $\Delta_x$  and  $\Delta_y$  in the  $x$  and  $y$  directions, respectively. The co-occurrence matrix  $C(i, j | \Delta_x, \Delta_y)$  is defined as

$$C(i, j | \Delta_x, \Delta_y) = \left| \{(p, q), (p + \Delta_x, q + \Delta_y) : I(p, q) = i, I(p + \Delta_x, q + \Delta_y) = j\} \right| \quad [1]$$

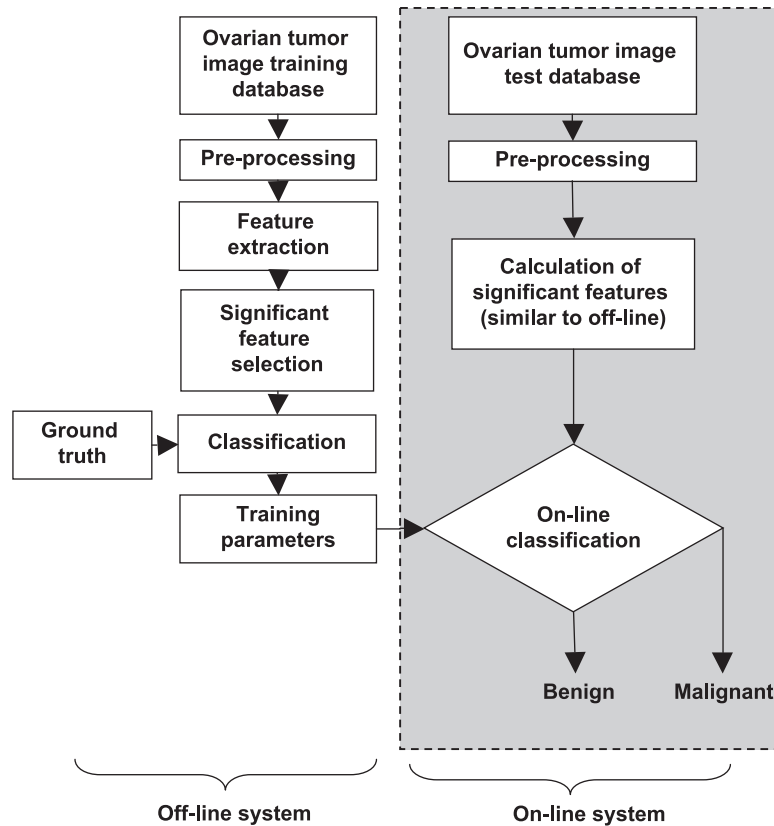


Figure 2: Block diagram of the proposed system GyneScan™ for ovarian tumor detection.

where  $(p, q), (p + \Delta_x, q + \Delta_y) \in M \times N$ ,  $d = (\Delta_x, \Delta_y)$  and  $|\odot|$  denotes the cardinality of a set. The probability that a gray level pixel  $i$  is at a distance  $(\Delta_x, \Delta_y)$  away from the gray level pixel  $j$  is given by

$$P(i, j) = \frac{C(i, j)}{\sum C(i, j)} \quad [2]$$

The following features were computed from the co-occurrence matrix:

- **First order statistical features:** Based on the first order statistics, five features were extracted from the pre-processed fundus image  $f(x, y)$ . They are mean, variance, skewness, kurtosis and energy. Table I presents the description of these features.
- **GLCM based textural features:** Let  $I(i, j)$  denote the original fundus image (normal or abnormal) and let the image have distinct gray level intensities. Firstly, we calculated the GLCM of order  $N \times N$ , where  $N$  refers the number of gray levels. An element of the GLCM matrix  $(i, j, d, \theta)$  is defined as the joint probability of the gray levels  $I$  and  $j$  separated by distance  $d$  and along direction  $\theta$ . To reduce the computation, we have

Table I  
Definition of first order statistical features.

S. No.	Features	Description
1	Mean (m)	$m = \frac{\sum_{x=1}^M \sum_{y=1}^N f(x, y)}{M \times N}$
2	Variance ( $\sigma^2$ )	$\sigma^2 = \frac{\sum_{x=1}^M \sum_{y=1}^N \{f(x, y) - m\}^2}{M \times N}$
3	Skewness ( $S_k$ )	$S_k = \frac{1}{M \times N} \frac{\sum_{x=1}^M \sum_{y=1}^N \{f(x, y) - m\}^3}{\sigma^3}$
4	Kurtosis ( $K_t$ )	$K_t = \frac{1}{M \times N} \frac{\sum_{x=1}^M \sum_{y=1}^N \{f(x, y) - m\}^4}{\sigma^4}$
5	Energy (E)	$E = \sum_{x=1}^M \sum_{y=1}^N f(x, y)^2$

used  $\theta$  as  $0^\circ, 45^\circ, 90^\circ$ , and  $135^\circ$ , and  $d$  is defined as the Manhattan or city block distance based on this GLCM. These features are mathematically defined as shown in Table II.

**Table II**  
Description of GLCM based textural features.

S. No.	Haralick feature	Description
1	Contrast	$I_{con} = \sum_{n=0}^{N-1} n^2 \left\{ \sum_{i=0}^N \sum_{j=0}^N P(i, j) \right\}$
2	Autocorrelation	$I_{autocor} = \sum_{i=0}^{N-1} \sum_{j=0}^{N-1} (ij)P(i, j)$
3	Maximum probability	$I_{mpb} = \sum_{i=0}^{N-1} \sum_{j=0}^{N-1} \max P(i, j)$
4	Dissimilarity	$I_{dsmrt} = \sum_{i=0}^{N-1} \sum_{j=0}^{N-1}  i - j  P(i, j)$
5	Homogeneity	$I_{hmg} = \sum_{i=0}^{N-1} \sum_{j=0}^{N-1} \frac{1}{1 + (i - j)^2} P(i, j)$
6	Entropy	$I_{Entr} = - \sum_{i=0}^{N-1} \sum_{j=0}^{N-1} P(i, j) \log(P(i, j))$
7	Energy	$I_{Enrg} = \sum_{i=0}^{N-1} \sum_{j=0}^{N-1} P(i, j)^2$
8	Correlation	$I_{cor} = \frac{\sum_{i=0}^{N-1} \sum_{j=0}^{N-1} (i, j)P(i, j) - \mu_x \mu_y}{\sigma_x \sigma_y}$ where $\sigma_x, \sigma_y, \mu_x, \mu_y$ are the standard deviations and means of $P_x, P_y$ . $P_x, P_y$ are the partial probability density functions. $p_x(i) = i^{th}$ entry in the marginal-probability matrix obtained by summing the rows of $P(i, j)$
9	Cluster shade	$I_{clsh} = \sum_{i=0}^{N-1} \sum_{j=0}^{N-1} \{i + j - \mu_x - \mu_y\}^3 \times P(i, j)$
10	Variance	$I_{variance} = \sum_{i=0}^{N-1} \sum_{j=0}^{N-1} (i - \mu)^2 \log(P(i, j))$ where $\mu = \text{mean of } P(i, j)$
11	Sum average	$I_{savg} = \sum_{i=2}^{2N} iP_{x+y}(i)$
12	Sum entropy	$I_{sentr} = - \sum_{i=2}^{2N} P_{x+y}(i) \log\{P_{x+y}(i)\}$
13	Sum variance	$I_{svar} = \sum_{i=2}^{2N} (i - I_{sentr})^2 P_{x+y}(i)$
14	Difference variance	$I_{dvar} = \sum_{i=2}^{2N} (i - I_{savg})^2 P_{(x-y)}(i)$
15	Difference entropy	$I_{dentr} = - \sum_{i=0}^{N-1} P_{x-y}(i) \log\{P_{x-y}(i)\}$
16	Information correlation measure 1	$I_{IMC1} = \frac{HXY - HXY_1}{\max(HX - HY)}$
17	Information correlation measure 2	$I_{IMC2} = \sqrt{1 - \exp[-2(HXY_2 - HXY)]}$ where $HX$ and $HY$ are the entropies for $P_x$ and $P_y$ $HX = - \sum_{i=0}^{N-1} P_x(i) (\log(P_x(i)))$ $HY = - \sum_{j=0}^{N-1} P_y(j) (\log(P_y(j)))$ $HXY = - \sum_{i,j=0}^{N-1} P(i, j) (\log(P(i, j)))$ $HXY_1 = - \sum_{i,j=0}^{N-1} P(i, j) \log(P_x(i)P_y(j))$ $HXY_2 = - \sum_{i,j=0}^{N-1} P_x(i)P_y(j) \log(P_x(i)P_y(j))$

- **Run length matrix based texture features:** Galloway (39) observed that in coarse texture, long gray level runs may exist more frequently as compared to fine texture which generally contains short runs. Galloway

**Table III**

Description of run length matrix based textural features.

S.No	Feature	Description
1	Short Run Emphasis (SRE)	$SRE = \frac{\sum_{i=1}^{N_x} \sum_{j=1}^{N_y} R(i, j)}{\sum_{i=1}^{N_x} \sum_{j=1}^{N_y} j^2}$
2	Long Run Emphasis (LRE)	$LRE = \frac{\sum_{i=1}^{N_x} \sum_{j=1}^{N_y} j^2 R(i, j)}{\sum_{i=1}^{N_x} \sum_{j=1}^{N_y} R(i, j)}$
3	Gray-level Non-uniformity (GLNU)	$GLNU = \frac{\sum_{i=1}^{N_x} \left( \sum_{j=1}^{N_y} R(i, j) \right)^2}{\sum_{i=1}^{N_x} \sum_{j=1}^{N_y} R(i, j)}$
4	Run length Non-uniformity (RLNU)	$RLNU = \frac{\sum_{j=1}^{N_x} \left( \sum_{i=1}^{N_y} R(i, j) \right)^2}{\sum_{i=1}^{N_x} \sum_{j=1}^{N_y} R(i, j)}$
5	Run Percentage (RP)	$RP = \frac{\sum_{i=1}^{N_x} \sum_{j=1}^{N_y} R(i, j)}{P}$ Here P is the total number of image pixels point.
6	Low Gray-level Run Emphasis (LGRE)	$LGRE = \frac{\sum_{i=1}^{N_x} \sum_{j=1}^{N_y} \frac{R(i, j)}{i^2}}{\sum_{i=1}^{N_x} \sum_{j=1}^{N_y} R(i, j)}$
7	High Gray-level Run Emphasis (HGRE)	$HGRE = \frac{\sum_{i=1}^{N_x} \sum_{j=1}^{N_y} R(i, j) \cdot i^2}{\sum_{i=1}^{N_x} \sum_{j=1}^{N_y} R(i, j)}$
8	Short Run Low Gray-level Run Emphasis (SRLGE)	$SRLGE = \frac{\sum_{i=1}^{N_x} \sum_{j=1}^{N_y} \frac{R(i, j)}{i^2 \cdot j^2}}{\sum_{i=1}^{N_x} \sum_{j=1}^{N_y} R(i, j)}$
9	Short Run High Gray-level Run Emphasis (SRHGE)	$SRHGE = \frac{\sum_{i=1}^{N_x} \sum_{j=1}^{N_y} \frac{R(i, j) \cdot i^2}{j^2}}{\sum_{i=1}^{N_x} \sum_{j=1}^{N_y} R(i, j)}$
10	Long Run Low Gray-level Run Emphasis (LRLGE)	$LRLGE = \frac{\sum_{i=1}^{N_x} \sum_{j=1}^{N_y} \frac{R(i, j) \cdot j^2}{i^2}}{\sum_{i=1}^{N_x} \sum_{j=1}^{N_y} R(i, j)}$
11	Long Run High Gray-level Run Emphasis (LRHGE)	$LRHGE = \frac{\sum_{i=1}^{N_x} \sum_{j=1}^{N_y} R(i, j) \cdot j^2 \cdot i^2}{\sum_{i=1}^{N_x} \sum_{j=1}^{N_y} R(i, j)}$

(39) studied the application of run length matrix for texture feature extraction. Run length matrix,  $R(i, j)$ , records the frequency that  $j$  points with a gray level  $i$  continue in the direction  $\theta$ . Here, we consider the run lengths matrices for angles  $\theta = 0^\circ, 45^\circ, 90^\circ, 135^\circ$ . The following features, shown in Table III, were calculated from the run length matrix.

*Classifiers*

**Support Vector Machine (SVM):** It is an efficient classifier especially for the data distributed in higher dimensions. It works by linearly separating two data points belonging to two different classes by a hyperplane (40). Non-linear classification can be performed using kernel functions. It can directly solve two class problems but multi-class solution can also be obtained by breaking them into several two class problems. We have used the linear kernel, quadratic kernel, polynomial kernel of order 1, 2, and 3 and the Radial Basis Function (RBF) kernels in this work.

**Decision Tree (DT):** Computationally cheap and user friendly decision trees have been used. These are one of the easiest supervised learners which follow tree structure for depicting decisions (41). Every parent node in the tree is an objective node which branches into child nodes as either a decision of belongingness of data or another objective node or both. A statistical property called information gain is calculated which is a measure of separation between training examples and target classification.

**k-Nearest Neighbor (KNN):** Nearest neighbor is a non-parametric algorithm. In this algorithm it is assumed that a test observation closer to a trained labeled data should have same belongingness (42). The closeness is calculated by distance metrics. In KNN, 'k' implies the number of observations near to the test point. The value  $k$  should be tactically selected and it should be small enough to contain only relevant data points and large enough to not miss any data points which would decide its belongingness to a class. This classifier can perform well even with lesser training data.

**Naive Bayes (NB):** Bayes' rule says that posterior probability is proportional to prior probability times likelihood (43). Naïve Bayes algorithm is based on the Bayes' rule but here it is assumed that features are independent of each other *i.e.* presence of one feature is totally independent of presence of another feature. Even maximum likelihood is also used for parameter estimation in several applications. As they are based on probabilistic model they are very good supervised learners and can be trained even with lesser data.

**Probabilistic Neural Network (PNN):** It is a feed-forward network of multiple layers where the input layer, pattern layer, summation/category layer and output layer are arranged

sequentially to receive inputs from previous layer and forward the output to the input of next layer (44). Every input in the input layer is fed to every node in the pattern layer; here, unlike common back-propagation algorithm where sigmoid function is used for activation, a non-linear function is used.

*Feature Selection, Classification, Probabilistic Neural Network (PNN) Parameter Tuning and Genetic Algorithm*

We used the Maximum Relevance Minimum Redundancy (mRMR) - Mutual Information Quotient (MIQ) method as the feature selection method. This technique relates the highest relevance of a feature to its class (45). It does that by determining

mutual information (a statistical measure) between (a) target feature and its class, which should be maximized for class determination and (b) between two features, which should be minimized to remove information redundancy. They together are known as mRMR. A difference operator called Mutual Information Quotient (MIQ) is introduced to optimize both the relevance and redundancy values. The extracted features were evaluated and further selected using student's *t*-test, which was used to assess whether the means of a feature in two groups are statistically different from each other by comparing with *p*-values at less than 0.05 which were considered clinically significant. The classifier robustness was evaluated using ten-fold cross validation technique.

**Table IV**  
Results of (Mean ± SD) for various features extracted.

	Rank of feature using mRMR-MIQ	Benign		Malignant		<i>p</i> -value
		Mean ± SD		Mean ± SD		
Autocorrelation	1	18.962 ± 4.132		18.030 ± 3.516		<0.0001
Homogeneity 90	27	0.705 ± 0.054		0.726 ± 0.066		<0.0001
Dissimilarity	3	0.799 ± 0.180		0.720 ± 0.209		<0.0001
Max probability	2	0.151 ± 0.122		0.179 ± 0.150		<0.0001
Contrast 0	13	0.930 ± 0.313		0.813 ± 0.301		<0.0001
Information correlation measure 2	12	0.801 ± 0.065		0.829 ± 0.068		<0.0001
Sum variance	8	43.727 ± 9.655		41.503 ± 7.589		<0.0001
Cluster shade	5	12.815 ± 19.309		20.148 ± 29.866		<0.0001
Correlation 90	19	0.799 ± 0.080		0.831 ± 0.087		<0.0001
Energy 0	21	0.076 ± 0.051		0.092 ± 0.090		<0.0001
Energy 135	24	0.061 ± 0.050		0.079 ± 0.091		<0.0001
Energy 90	23	0.067 ± 0.050		0.084 ± 0.091		<0.0001
Skewness	29	0.264 ± 0.326		0.333 ± 0.362		<0.0001
Homogeneity 45	26	0.661 ± 0.063		0.687 ± 0.076		<0.0001
Energy 45	22	0.061 ± 0.050		0.079 ± 0.091		<0.0001
Run length non-uniformity	35	3538.049 ± 981.493		3056.297 ± 1039.805		<0.0001
Short run low gray-level run emphasis	38	0.103 ± 0.117		0.111 ± 0.102		0.047
Variance	31	4600.694 ± 613.812		4817.160 ± 714.229		<0.0001
Kurtosis	30	2.240 ± 0.413		2.292 ± 0.457		0.002
Long run high gray-level run emphasis	40	6240082.394 ± 10506429.767		12769818.857 ± 12309279.552		<0.0001
Gray-level non-uniformity	33	14966.417 ± 10250.377		24261.805 ± 15036.827		<0.0001
Run percentage	34	0.629 ± 0.148		0.567 ± 0.148		<0.0001
High gray-level run emphasis	37	3369.684 ± 2831.230		5109.719 ± 2934.456		<0.0001
Low gray-level run emphasis	36	3.714 ± 7.851		5.168 ± 6.819		<0.0001
Short run emphasis	32	0.768 ± 0.050		0.747 ± 0.065		<0.0001
Long run low gray-level run emphasis	39	9904.270 ± 27160.338		14878.838 ± 23762.561		<0.0001
Entropy	4	3.320 ± 0.323		3.212 ± 0.432		<0.0001
Sum average	6	7.877 ± 1.231		7.580 ± 1.145		<0.0001
Sum entropy	7	2.520 ± 0.162		2.487 ± 0.253		<0.0001
Difference variance	9	1.550 ± 0.487		1.330 ± 0.535		<0.0001
Difference entropy	10	1.158 ± 0.135		1.088 ± 0.181		<0.0001
Information correlation measure 1	11	-0.292 ± 0.092		-0.336 ± 0.111		<0.0001
Contrast 45	14	1.886 ± 0.600		1.615 ± 0.659		<0.0001
Contrast 90	15	1.485 ± 0.488		1.273 ± 0.546		<0.0001
Contrast 135	16	1.899 ± 0.593		1.619 ± 0.655		<0.0001
Correlation 0	17	0.875 ± 0.049		0.893 ± 0.050		<0.0001
Correlation 45	18	0.745 ± 0.098		0.786 ± 0.106		<0.0001
Correlation 135	20	0.744 ± 0.097		0.785 ± 0.106		<0.0001
Homogeneity 0	25	0.753 ± 0.049		0.772 ± 0.057		<0.0001
Homogeneity 135	28	0.661 ± 0.062		0.687 ± 0.075		<0.0001

**Table V**  
Results of average accuracy, sensitivity, specificity and PPV for various classifiers.

Classifiers	No. of features	Accuracy (%)	PPV (%)	Sensitivity (%)	Specificity (%)
SVM, RBF	31	100.00	100.00	100.00	100.00
SVM, linear	40	84.73	87.59	81.00	88.46
SVM, quadratic	38	100.00	100.00	100.00	100.00
SVM, poly3	15	100.00	100.00	100.00	100.00
Decision tree	22	98.54	98.92	98.15	98.92
KNN	11	100.00	100.00	100.00	100.00
Naïve bayes	3	67.35	69.93	60.62	74.08
PNN	11	100.00	100.00	100.00	100.00

## Results

### Selected Features

In our work, 40 out of 42 extracted texture features were clinically significant ( $p < 0.0001$ ). Table IV also shows the rank of each feature (mean and standard deviation) using the mRMR-MIQ feature selection method.

### Classification Results

To evaluate the classifiers, we used ten-fold stratified cross validation technique. The entire dataset (1300 benign and 1300 malignant) was divided into ten equal groups, with each group containing the equal number of images from each class. During the first trial, nine groups were used to train the classifier and the remaining one part was used to test the classifiers and to obtain the performance measures. This procedure was repeated nine more times by using a different test set each time. The averages of the performance metrics (sensitivity, specificity, diagnostic accuracy, and PPV) obtained in all the iterations are reported as the overall performance metrics (Table V). It is evident from Table V that among all the classifiers, the PNN and KNN classifiers presented 100% average accuracy, sensitivity, specificity, and PPV using only 11 significant features.

### Discussion

Besides ultrasonography, another most commonly used technique for detecting ovarian cancer is to determine the levels of a tumor marker called Cancer-Antigen 125 (CA125). However, CA125 marker has been found to be elevated only in 50% of stage I cancers (46), and also CA125 can be increased in pancreatic and uterine malignancies, and frequently in benign conditions also (47). There is limited literature on CAD based studies for ovarian tumor classification. In Table VI, we present a summary of the findings of these published studies. It can be seen that the MS based studies (26-28, 48, 49) have resulted in high accuracies. However, they are limited by the cost and availability of

the data analysis equipment. Menon (50) examined women with elevated CA125 levels and concluded that sensitivity of ultrasound reading can be increased by the usage of ovarian morphology and PPV can be increased by the use of complex ovarian morphology. Tailor *et al.* (51) and Biagiotti *et al.* (29) used operator suggested features (Table VI), and hence, are subjective in nature (features). The techniques developed by Zimmer *et al.* (31) and Lucidarme *et al.* (30) presented accuracies of only 70% and 91.73%, respectively.

Recently, our group (52) presented a classification model to automatically discriminate the malignant and benign ovarian tumors in ultrasound images. We used texture features based on Laws Texture Energy and Local Binary Patterns extracted from 1000 benign and 1000 malignant images in a SVM classifier, and obtained an accuracy of 99.9%, sensitivity of 100% and specificity of 99.8% using 2000 ultrasound images. In another study (53), we extracted Hu's invariant moments, Gabor transform parameters and entropies from 1300 benign and 1300 malignant ovarian tumors. Significant features were fed to the PNN classifier fine-tuned by genetic algorithm (GA) achieved an average classification accuracy of 99.8%, sensitivity of 99.2% and specificity of 99.6% at  $\sigma = 0.264$ . In our last study (54), we extracted features based on the textural changes and higher-order spectra from 1000 images in each category (benign and malignant), and used them in a DT classifier. An accuracy of 97%, sensitivity of 94.3%, and specificity of 99.7% was obtained. After evaluating a variety of features that quantify the gray-level intensity variations in the ultrasound images, we concluded that there is still room for improvement in the accuracy. Therefore, we studied texture features based on first order statistics, GLCM and run length matrices in this work, and using 11 significant features in KNN/PNN classifiers, we were able to achieve 100% classification accuracy in detecting ovarian tumor. The following are some key features of our proposed technique:

- Since the proposed *GyneScan* algorithm is automated, the final diagnosis result is objective and does not require specific training or expertise to understand the end-results.



**Table VI**  
Summary of results of CAD based studies for ovarian tumor classification.

Literature	No. of samples	Features	Classifier	Performance
Renz <i>et al.</i> (25)	Benign, early stage and late stage cancers (55 cases)	Blood test data and age	Multilayer perceptron	Accuracy: 92.9%
Assareh and Moradi (48)	Dataset 1: 91 normal, 162 cancers Dataset 2: 100 normal, 16 benign and 100 cancers	Three significant biomarkers from protein mass spectra	Two fuzzy linguistic rules	Dataset 1: Accuracy: 100% Dataset 2: Accuracy: 86.36%
Tan <i>et al.</i> (26)	24 normal, 30 cancers	DNA micro-array, blood test, and proteomics data	Complementary Learning Fuzzy Neural Network	Accuracy: 84.72%
Tang <i>et al.</i> (27)	95 normal, 121 cancers	Four statistical moments (mean, variance, skewness and kurtosis) obtained from SELDI-TOF mass spectroscopy data	Kernel partial least square classifier	Accuracy: 99.35% Sensitivity: 99.5% Specificity: 99.16%
Petricoin (28)	66 benign, 50 cancers	Proteomic spectra	Genetic algorithm with self organizing cluster analysis	Sensitivity: 100% Specificity: 95%
Taylor <i>et al.</i> (51)	52 benign, 15 cancers	Clinical and ultrasound based variables from TVUS images	Back propagation neural network	Sensitivity: 100% Specificity: 98.1%
Biagiotti <i>et al.</i> (29)	175 benign, 51 cancers	Age and parameters from TVUS images	Three layer back propagation network	Sensitivity: 96%
Zimmer <i>et al.</i> (31)	–	B-scan ultrasound images	Morphological Analysis	Accuracy: 70%
Lucidarme <i>et al.</i> (30)	234 benign, 141 cancers	Quantification of tissue disorganization in backscattered ultrasound (3D TVUS)	Ovarian HistoScanning (OHS) system	Sensitivity: 98% Specificity: 88% Accuracy: 91.73%
Acharya <i>et al.</i> (52)	1000 benign, 1000 cancers	Local Binary Pattern + Law's Mask Energy	SVM classifier	Sensitivity: 100% Specificity: 99.8% Accuracy: 99.9%
Acharya <i>et al.</i> (53)	1300 benign, 1300 cancers	Hu's invariant moments + Gabor wavelet features + Entropies	PNN classifier, tuned with genetic algorithm	Sensitivity: 99.2% Specificity: 99.6% Accuracy: 99.8%
Acharya <i>et al.</i> (54)	1000 benign, 1000 cancers	Texture and higher-order spectra based features	DT classifier	Sensitivity: 94.3% Specificity: 99.7% Accuracy: 97.0%
Proposed method	1300 benign, 1300 cancers	Features based on first order statistics, GLCM and run length matrix	KNN/PNN classifiers	Sensitivity: 100% Specificity: 100% Accuracy: 100%

- b. Due to the use of a large sample size (2600 images) for the training and evaluation of classifiers, and also because of the use of stratified cross validation technique for data resampling, the classifiers are generalized to effectively handle new images.
- c. The accuracy was obtained using only 11 features, and hence there is no problem of curse of dimensionality that is an issue for MS data.
- d. The *GyneScan* system can be easily deployed on any computer and does not require expensive software. Since the algorithm works on ultrasound images which are now commonly acquired and affordable, the over-all set-up and use of the proposed system is cost-effective.
- e. Besides the afore-mentioned advantages, the key finding in this preliminary study is the algorithm's capability to detect ovarian tumor with a high accuracy of 100%.

On the limitations side, we understand the need for more validation using larger databases to establish the accuracy of the proposed CAD algorithm. Moreover, we propose to continue this study to 3D, where we use the spatial information of the 3D slices taken from a single patient for further analysis.

### Conclusion

In our earlier studies in the area of CAD based ovarian tumor classification, we found that the classification accuracy could be further improved. Therefore, in this work, we have proposed another CAD technique *GyneScan* that successfully captures the subtle variations in the gray-level intensity variations in the ultrasound images of benign and malignant ovarian tumors using several texture features based on first order statistics, Gray Level Co-occurrence Matrix and run

length matrix. On using 11 significant features extracted from 1300 benign and 1300 malignant images to train/test KNN/PNN classifiers, we were able to achieve 100% classification accuracy, sensitivity, specificity, and positive predictive value. Thus, the proposed technique could be a more objective adjunct method to detect the presence/absence of ovarian tumor.

### Conflict of Interest

The authors declare the absence of any conflict of interest related to the present paper. The results are novel and original.

### References

- Riihimaki M, Hemminki A, Sundquist K & Hemminki K. Time trends in survival from cancer of unknown primary: small steps forward. *Eur J Cancer* 49, 2403-2410 (2013). DOI: 10.1016/j.ejca.2013.02.022
- Ibeanu OA & Díaz-Montes TP. Outcomes in ovarian cancer among hispanic women living in the United States: a population-based analysis. *Pathology Res Intl* 2013, 5 (2013). DOI: 10.1155/2013/672710
- Hall M, Gourley C, McNeish I, Ledermann J, Gore M, Jayson G, Perren T, Rustin G & Kaye S. Targeted anti-vascular therapies for ovarian cancer: current evidence. *Br J Cancer* 108, 250-258 (2013). DOI: 10.1038/bjc.2012.541
- Attard G & Kaye SB. Identifying prognostic signatures in the blood of ovarian cancer patients. *Gynecol Oncol* 128, 1-2 (2013). DOI: 10.1016/j.ygyno.2012.11.011
- Morris RT & Monk BJ. Ovarian cancer: relevant therapy, not timing, is paramount. *The Lancet* 376, 1120-1122 (2010). DOI: 10.1016/S0140-6736(10)61515-2
- Wu CC, Lee CN, Chen TM, Lai JI, Hsieh CY & Hsieh FJ. Factors contributing to the accuracy in diagnosing ovarian malignancy by color Doppler ultrasound. *Obstet Gynecol* 84, 605-608 (1994).
- Horner MJ, Ries LAG, Krapcho M, Neyman N, Aminou R, Howlander N, Altekruse SF, Feuer EJ, Huang L, Mariotto A, Miller BA, Lewis DR, Eisner MP, Stinchcomb DG & Edwards BK. *SEER Cancer Statistics Review, 1975-2006*, [http://seer.cancer.gov/csr/1975\\_2006/](http://seer.cancer.gov/csr/1975_2006/), (2009).
- Predanic M, Vlahos N, Pennisi JA, Moukhtar M & Aleem FA. Color and pulsed doppler sonography, gray-scale imaging, and serum CA 125 in the assessment of adnexal disease. *Obstet Gynecol* 88, 283-288 (1996). DOI: 10.1016/0029-7844(96)00152-4
- Iyer VR & Lee SI. MRI, CT, and PET/CT for ovarian cancer detection and adnexal lesion characterization. *AJR Am J Roentgenol* 194, 311-321 (2010). DOI: 10.2214/AJR.09.3522
- Alcazar JL, Pascual MA, Olartecoechea B, Graupera B, Auba M, Ajossa S, Hereter L, Julve R, Gaston B, Peddes C, Sedda F, Piras A, Saba L & Guerriero S. IOTA simple rules for discriminating between benign and malignant adnexal masses: prospective external validation. *Ultrasound Obstet Gynecol* 42, 467-471 (2013). DOI: 10.1002/uog.12485
- Frangioni JV. New technologies for human cancer imaging. *J Clin Oncol* 26, 4012-4021 (2008). DOI: 10.1200/JCO.2007.14.3065
- Sohaib SA & Reznick RH. MR imaging in ovarian cancer. *Cancer Imaging* 7, S119-129 (2007). DOI: 10.1102/1470-7330.2007.9046
- Anderiesz C & Quinn MA. Screening for ovarian cancer. *The Medical Journal of Australia* 178, 655-656 (2003).
- Jeong YY, Outwater EK & Kang HK. Imaging evaluation of ovarian masses. *Radiographics: A Review Publication of the Radiological Society of North America, Inc* 20, 1445-1470 (2000).
- Barua A, Bitterman P, Bahr JM, Basu S, Sheiner E, Bradaric MJ, Hales DB, Luborsky JL & Abramowicz JS. Contrast-enhanced sonography depicts spontaneous ovarian cancer at early stages in a preclinical animal model. *J Ultrasound Med* 30, 333-345 (2011).
- Saba L, Guerriero S, Sulcis R, Virgilio B, Melis G & Mallarini G. Mature and immature ovarian teratomas: CT, US and MR imaging characteristics. *Eur J Radiol* 72, 454-463 (2009). DOI: 10.1016/j.ejrad.2008.07.044
- Pascual MA, Graupera B, Hereter L, Rotili A, Rodriguez I & Alcazar JL. Intra- and interobserver variability of 2D and 3D transvaginal sonography in the diagnosis of benign versus malignant adnexal masses. *J Clin Ultrasound* 39, 316-321 (2011). DOI: 10.1002/jcu.20808
- Guerriero S, Alcazar JL, Pascual MA, Ajossa S, Gerada M, Bargellini R, Virgilio B & Melis GB. Intraobserver and interobserver agreement of grayscale typical ultrasonographic patterns for the diagnosis of ovarian cancer. *Ultrasound Med Biol* 34, 1711-1716 (2008). DOI: 10.1016/j.ultrasmedbio.2008.04.007
- Guerriero S, Alcazar JL, Pascual MA, Ajossa S, Graupera B, Hereter L & Melis GB. The diagnosis of ovarian cancer: is color Doppler imaging reproducible and accurate in examiners with different degrees of experience? *J Womens Health (Larchmt)* 20, 273-277 (2011). DOI: 10.1089/jwh.2010.2277
- Timmerman D, Schwarzler P, Collins WP, Claerhout F, Coenen M, Amant F, Vergote I & Bourne TH. Subjective assessment of adnexal masses with the use of ultrasonography: an analysis of interobserver variability and experience. *Ultrasound Obstet Gynecol* 13, 11-16 (1999). DOI: 10.1046/j.1469-0705.1999.13010011.x
- Kim KA, Park CM, Lee JH, Kim HK, Cho SM, Kim B & Seol HY. Benign ovarian tumors with solid and cystic components that mimic malignancy. *American Journal of Roentgenology* 182, 1259-1265 (2004). DOI: 10.2214/ajr.182.5.1821259
- Molinari F, Mantovani A, Deandrea M, Limone P, Garberoglio R & Suri JS. Characterization of single thyroid nodules by contrast-enhanced 3-D ultrasound. *Ultrasound Med Biol* 36, 1616-1625 (2010). DOI: 10.1016/j.ultrasmedbio.2010.07.011
- Acharya UR, Vinitha Sree S, Krishnan MM, Molinari F, Garberoglio R & Suri JS. Non-invasive automated 3D thyroid lesion classification in ultrasound: a class of ThyroScan systems. *Ultrasonics* 52, 508-520 (2012). DOI: 10.1016/j.ultras.2011.11.003
- Saba L, Gao H, Acharya UR, Sannia S, Ledda G & Suri JS. Analysis of carotid artery plaque and wall boundaries on CT images by using a semi-automatic method based on level set model. *Neuroradiology* 54, 1207-1214 (2012). DOI: 10.1007/s00234-012-1040-x
- Renz C, Rajapakse JC, Razvi K & Liang SKC. in *Neural Information Processing, 2002. ICONIP '02. Proceedings of the 9th International Conference on*. 809-813, vol. 802.
- Tan TZ, Quek C, Ng GS & Razvi K. Ovarian cancer diagnosis with complementary learning fuzzy neural network. *Artif Intell Med* 43, 207-222 (2008). DOI: 10.1016/j.artmed.2008.04.003
- Tang KL, Li TH, Xiong WW & Chen K. Ovarian cancer classification based on dimensionality reduction for SELDI-TOF data. *BMC Bioinformatics* 11, 109 (2010). DOI: 10.1186/1471-2105-11-109
- Petricoin EF, Ardekani AM, Hitt BA, Levine PJ, Fusaro VA, Steinberg SM, Mills GB, Simone C, Fishman DA, Kohn EC & Liotta LA. Use of proteomic patterns in serum to identify ovarian cancer. *Lancet* 359, 572-577 (2002). DOI: 10.1016/S0140-6736(02)07746-2
- Biagiotti R, Desii C, Vanzi E & Gacci G. Predicting ovarian malignancy: application of artificial neural networks to transvaginal and color Doppler flow US. *Radiology* 210, 399-403 (1999). DOI: <http://dx.doi.org/10.1148/radiology.210.2.r99fe18399>
- Lucidarme O, Akakpo JP, Granberg S, Sideri M, Levavi H, Schneider A, Autier P, Nir D & Bleiberg H. A new computer-aided diagnostic tool for non-invasive characterisation of malignant ovarian masses: results of a multicentre validation study. *Eur Radiol* 20, 1822-1830 (2010). DOI: 10.1007/s00330-010-1750-6

31. Zimmer Y, Tepper R & Akselrod S. An automatic approach for morphological analysis and malignancy evaluation of ovarian masses using B-scans. *Ultrasound Med Biol* 29, 1561-1570 (2003). DOI: 10.1016/j.ultrasmedbio.2003.08.013
32. Bellman RE. *Dynamic Programming*. (Dover Publications, 2003).
33. Hata T, Yanagihara T, Hayashi K, Yamashiro C, Ohnishi Y, Akiyama M, Manabe A & Miyazaki K. Three-dimensional ultrasonographic evaluation of ovarian tumours: a preliminary study. *Hum Reprod* 14, 858-861 (1999).
34. Jokubkiene L, Sladkevicius P & Valentin L. Does three-dimensional power Doppler ultrasound help in discrimination between benign and malignant ovarian masses? *Ultrasound Obstet Gynecol* 29, 215-225 (2007). DOI: 10.1002/uog.3922
35. Alcázar JL & Castillo G. Comparison of 2-dimensional and 3-dimensional power-Doppler imaging in complex adnexal masses for the prediction of ovarian cancer. *Am J Obstet Gynecol* 192, 807-812 (2005). DOI: 10.1016/j.ajog.2004.10.630
36. Laban M, Metawee H, Elyan A, Kamal M, Kamel M & Mansour G. Three-dimensional ultrasound and three-dimensional power Doppler in the assessment of ovarian tumors. *Int J Gynaecol Obstet* 99, 201-205 (2007). DOI: 10.1016/j.ijgo.2007.03.027
37. Cohen LS, Escobar PF, Scharm C, Glimco B & Fishman DA. Three-dimensional power Doppler ultrasound improves the diagnostic accuracy for ovarian cancer prediction. *Gynecol Oncol* 82, 40-48 (2001). DOI: 10.1006/gyno.2001.6253
38. Haralick RM, Shanmugam K & Dinstein IH. Textural Features for Image Classification. *IEEE Trans Syst Man, Cybern B, Cybern SMC* 3, 610-621 (1973). DOI: 10.1109/tsmc.1973.4309314
39. Galloway MM. Texture analysis using gray level run lengths. *Comput Gr Image Process* 4, 172-179 (1975). DOI: 10.1016/S0146-664X(75)80008-6.
40. Vapnik V. *The Nature of Statistical Learning Theory* (Springer, 2000).
41. Quinlan JR. Induction of decision trees. *Mach Learn* 1, 81-106 (1986). DOI: 10.1007/bf00116251.
42. Fix E & Hodges JL. *Discriminatory Analysis: Nonparametric Discrimination: Consistency Properties* (USAF School of Aviation Medicine, 1951).
43. Duda RO & Hart PE. *Pattern Classification and Scene Analysis* (Wiley, 1973).
44. Specht DF. Probabilistic neural networks. *Neural Netw* 3, 109-118 (1990). DOI: 10.1016/0893-6080(90)90049-q
45. Peng H, Fulmi L & Ding C. Feature selection based on mutual information criteria of max-dependency, max-relevance, and min-redundancy. *IEEE Trans Pattern Anal Mach Intell* 27, 1226-1238 (2005). DOI: 10.1109/tpami.2005.159.
46. Bast RC, Jr., Badgwell D, Lu Z, Marquez R, Rosen D, Liu J, Baggerly KA, Atkinson EN, Skates S, Zhang Z, Lokshin A, Menon U, Jacobs I & Lu K. New tumor markers: CA125 and beyond. *Int J Gynecol Cancer* 15, 274-281 (2005). DOI: 10.1111/j.1525-1438.2005.00441.x
47. Zaidi S. Fifty years of progress in gynecologic ultrasound. *International Journal of Gynaecology and Obstetrics: the Official Organ of the International Federation of Gynaecology and Obstetrics* 99, 195-197 (2007). DOI: 10.1016/j.ijgo.2007.08.002
48. Assareh A & Moradi MH. in *Computational Intelligence and Bioinformatics and Computational Biology, 2007. CIBCB '07. IEEE Symposium on*. 502-506.
49. Hui M, Wenxue H, Jialin S & Liqiang W. in *Bioinformatics and Biomedical Engineering, 2008. ICBBE 2008. The 2nd International Conference on*. 668-671.
50. Menon U, Talaat A, Rosenthal AN, Macdonald ND, Jeyerajah AR, Skates SJ, Sibley K, Oram DH & Jacobs IJ. Performance of ultrasound as a second line test to serum CA125 in ovarian cancer screening. *BJOG: an International Journal of Obstetrics and Gynaecology* 107, 165-169 (2000). DOI: 10.1111/j.1471-0528.2000.tb11685.x.
51. Tailor A, Jurkovic D, Bourne TH, Collins WP & Campbell S. Sonographic prediction of malignancy in adnexal masses using an artificial neural network. *Br J Obstet Gynaecol* 106, 21-30 (1999). DOI: 10.1111/j.1471-0528.1999.tb08080.x
52. Acharya UR, Sree SV, Krishnan MM, Saba L, Molinari F, Guerriero S & Suri JS. Ovarian tumor characterization using 3D ultrasound. *Technol Cancer Res Treat* 11, 543-552 (2012). DOI: 10.7785/tcrt.2012.500272
53. Acharya UR, Mookiah MR, Vinitha Sree S, Yanti R, Martis RJ, Saba L, Molinari F, Guerriero S & Suri JS. Evolutionary algorithm-based classifier parameter tuning for automatic ovarian cancer tissue characterization and classification. *Ultraschall Med* (2012). DOI: 10.1055/s-0032-1330336
54. Acharya UR, Sree SV, Saba L, Molinari F, Guerriero S & Suri JS. Ovarian tumor characterization and classification using ultrasound—a new online paradigm. *J Digit Imaging*. 26, 544-553 (2013). DOI: 10.1007/s10278-012-9553-8.

Received: October 8, 2013; Revised: November 15, 2013;

Accepted: November 20, 2013